Electronic Supplementary Material (ESI) for Materials Chemistry Frontiers.

Carving Shell Thickness of Tungsten Trioxide Hollow Multi-Shelled Structures for Enhanced Photocatalytic Performance

Xing Zhang[1], Yilei He[1], Yanze Wei[2] and Ranbo Yu[1,3*].*

1 Department of Physical Chemistry, School of Metallurgical and Ecological Engineering, University of Science and Technology Beijing, 30, Xueyuan Road, Haidian District, Beijing 100083, China.

2 State Key Laboratory of Biochemical Engineering, Institute of Process Engineering, Chinese Academy of Sciences, 1 North 2nd Street, Zhongguancun, Haidian District, Beijing 100190, China.

3 Key Laboratory of Advanced Material Processing & Mold, Ministry of Education, Zhengzhou University, Zhengzhou 450002, P. R. China.

Supporting information:

Methods:

Regents: The chemical reagents including sucrose, anhydrous ethanol (EtOH), and acetone were purchased from the Sinopharm Chemical Reagent Co., Ltd. Tungsten chloride (WCl_6), silver nitrate ($AgNO_3$) and dimethylformamide (DMF) were purchased from Aladdin industrial Co., Ltd. All above chemicals were analytically pure and used as received without further purification. Deionized water was used in all experiments.

Fabrication of carbonaceous microspheres (CMSs) templates. CMS templates were fabricated through the hydrothermal polymerization reaction of sucrose according to previous literature. Briefly, 130 g of sucrose was slowly added into 250 ml of deionized water to form a transparent solution. Then the mixture was transferred into a 500 ml Teflon-lined autoclave, which was sealed and heated at 200 ºC for 123 min. For fabrication of CMS with larger size, the hydrothermal reaction time was elongated to 130 min. After the autoclave cooled to room temperature, the resulting brown product was collected by vacuum filtration, washed 6 times with deionized water and anhydrous ethanol and dried at 65 ºC for 12 h for further use.

Fabrication of thick-shelled WO_3 hollow multi-shelled structures (HoMSs). Sequential template approach (STA) was applied to fabricate thick-shelled WO_3 HoMSs by applying EtOH as the precursor solution. Typically, 0.6 g freshly prepared CMSs were added into 30 ml anhydrous ethanol containing 0.6 g of WCl_6 and the mixture was subjected to ultrasonic shaking for 5 min to ensure the uniform dispersion of CMS templates. Subsequently, the suspensions were placed in water bath with varying temperature (25-50 ºC) and time (6 h-12 h), followed by filtering and washing with anhydrous ethanol for several times, and drying in an oven at 65 ºC overnight. Finally, the resulted composites were heated to 450 ºC in Muffle furnace at the rate of 2 ºC min^{-1} and kept for 1 h to remove the templates. To get the WO_3 hollow structures with high crystallinity, the samples was further heated to 600 ºC and held for 1 h. For the synthesis of triple-shelled thick WO_3 HoMSs, CMSs templates with larger size were employed, following similar treating process.

Fabrication of thin-shelled WO_3 HoMSs. Although similar STA method was applied, the composition of precursor solution was critical in the preparation of thin-shelled WO_3 HoMSs. The shell number could be regulated by tuning the adsorption conditions, including the adsorption temperature and adsorption durations. Take the synthesis of thin triple-shelled WO_3 HoMSs as an

example, 0.24 g of WCl_6 was firstly dissolved in 30 mL mixed solution of EtOH and acetone (1:2) via ultrasonication. Then 0.6 g newly prepared CMSs were dispersed in the mixture, followed by adding for 3 h in 25 ºC water bath under stirring. Finally, the CMSs was separated by vacuum filtration, washed with anhydrous ethanol and dried at 65 ºC overnight. The calcination procedure was same as thick-shelled ones. The experimental details in the absorption process of different types of WO_3 hollow structures are shown in Supplementary Table 2.

Characterizations. Powder X-ray diffraction patterns were recorded by X-ray diffractometer (XRD, Panalytical X' Pert PRO MPD) with Cu-Kα radiation. SEM images of selected samples were taken on Zeiss Supra-55 field emission scanning electron microscopy operated at 15 kV. TEM images were taken on JEOL JEM-2100F field-emission high-resolution electron microscopy operated at 200 kV. X-ray photoelectron spectroscopy (XPS) were conducted on an ESCALab220i-XL electron spectrometer equipped with 300 W Al Kα radiation. The binding energies of the XPS date were standardized with respect to C 1s peak at 284.8 eV. Raman spectra were measured by using a Raman Spectrometer (Renishaw, in Via reflex) with excitation laser wavelength of 532 nm. Dynamic light scattering (DLS) measurement was conducted on Malvern Zetasizer Nano ZS90. All contact angle images were taken on contact angle analyzer (DM-701 Kyowa Interface Science Co., Ltd.) The thermogravimetric and differential thermal analysis (TGA-DTA) date of carbonaceous microspheres templates were collected by a DTA-60 (Shimadzu). Diffuse reflectance ultraviolet visible (UV-vis) of photocatalysts were obtained by a Varian Cary 5000UV-vis spectrometer with the reflectance standard of $BaSO_4$. Nitrogen adsorption-desorption isotherms were carried out on a Quantochrome Autosorb 1-MP sorption analysis. The Photoluminescence (PL) emission spectra were detected on a LP920 laser flash photolysis spectrometer at ambient temperature with the excitation wavelength of 325 nm. Photocurrent response performance of samples were recorded via a CHI760E electrochemical workstation equipped with a standard three-electron cell. The saturated Ag/AgCl and Pt wire were used as reference electrode and counter electrode. The catalysts were spread on the FTO glass through a printing method and used as working electrode in 0.2 M Na_2S and 0.04 M Na_2SO_3 mixed aqueous solution. Electrochemical impedance spectra (EIS) were recorded over a range from 0.1 to 2×10^5 Hz at a 0.02 V bias potential vs Ag/AgCl electrode. 0.5 M potassium phosphate buffer solution (pH = 7) was utilized as electrolyte.

Photocatalytic oxygen evolution performances. Photocatalytic oxygen evolution activities of the

obtained WO_3 HoMSs were carried out by using Labsolar 6A photocatalytic system (Beijing Perfectlight Technology Co. Ltd, China). $AgNO_3$ was used as sacrificial agent in photocatalytic water oxidation reaction. The system was composed of a closed gas circulation and a gas chromatography (GC-7900, Techcomp, China, TCD, argon as carrier gas). A 300 W Xe lamp (with a UV-cut filter $\lambda > 400$ nm) was used as the light source. Typically, 30 mg of the photocatalyst was dispersed in 100 ml 0.01 M $AgNO_3$ aqueous solution in a Pyrex glass reactor. During the measure process, the reactor cell was maintained at a constant temperature of 8 ºC under vigorous stirring. The amounts of gaseous products were online analyzed by gas chromatography at an interval of 30 min with reaction time for 4h. Besides, the apparent quantum efficiency (AQE) was determined using a 300 W Xe lamp equipped with additional monochromatic optical filter. 150 mg of the photocatalyst were used for each test. The AQE was calculated according to the formula:

AQE = (4 × the number of evolved O_2 molecules / number of incident photons) × 100%

Theoretical calculation and FDTD simulations. All DFT calculations in this work including crystal structures and optic properties of WO_3 HoMSs were conducted using the Vienna Ab Simulation Package via projector-augmented wave pseudopotentials. The plane-wave cutoff energy was 450 eV, a k-mesh of 4×4×4 gamma points was adopted to sample the Brillouin zone, and the Gaussian smearing was applied with a width of 0.05 eV. The hybrid density functional developed by Heyd, Scuseria and Ernzerhof (HSE) functional was used for all calculations in this paper. The frequency dependent dielectric function has been calculated based on the HSE functional, and the absorption coefficient, $\alpha(\omega)$ is defined by the following equation:

$$\alpha(\omega) = \sqrt{2}\,\omega\,(\sqrt{\varepsilon_1(\omega)^2 + \varepsilon_2(\omega)^2}) - \varepsilon_1(\omega)^{1/2}$$

The optical simulations were conducted using the FDTD solutions. The full-wave calculation was based on the finite difference method to solve Maxwell equations in the time domain. The optical properties of samples required by FDTD simulations were acquired from the DFT calculations. The radiuses and thicknessed of different shells were set according to the Table S3 and Table S4. A simulation box with dimensions of 3×3×3 μm was used. The resolution of the mesh grid was set to 2.5 nm across the simulation space. The light source ranged from 300 to 800 nm plane wave, normally incident to the materials. The refractive index of surrounding medium was set to be 1, which was the refractive index of air.

Results and Discussion

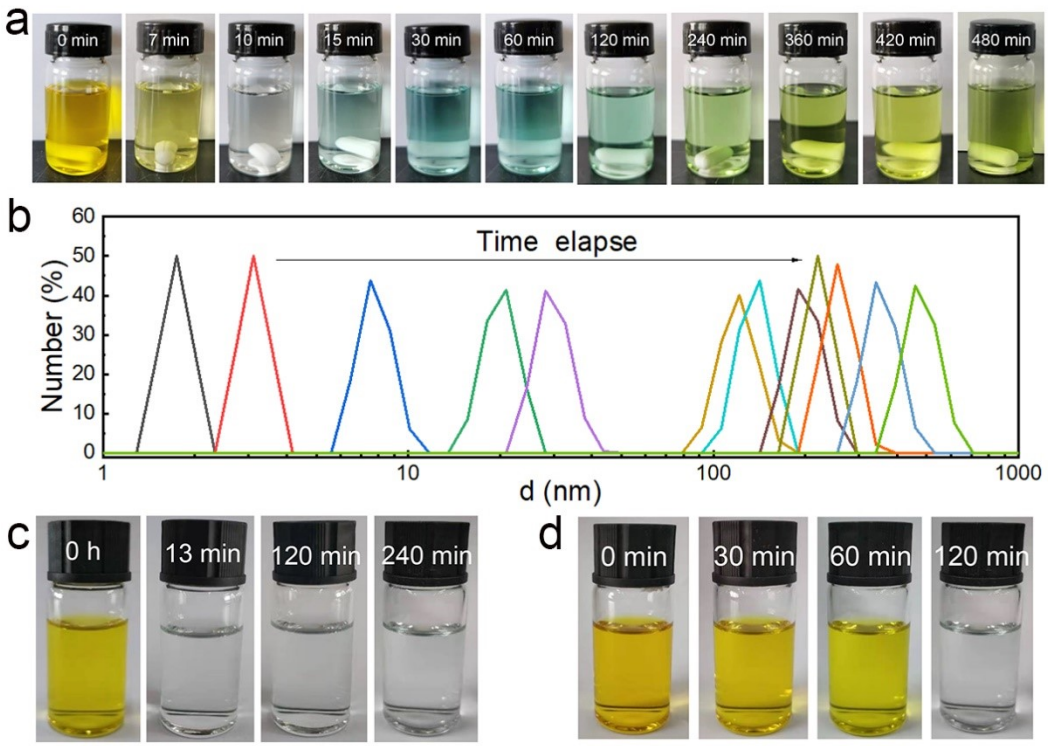

Figure S1. (a) Color changing of the WCl_6 solution caused by alcoholysis reaction (the concentration of WCl_6 is 0.01 M). (b) The change of the particle size distribution in WCl_6 solution via dynamic light scattering measurement. (c) Color changing of the WCl_6 solution (EtOH/Acetone=1) and (d) (EtOH/DMF=2). Experiments were performed under ambient condition.

As shown in **Figure S1a**, it could be clearly observed that the color changed from yellow (initial) to transparent (10 min), then to blue (15-120 min), and finally to yellow (>120 min), along with the apparently increased cluster size in the solution.

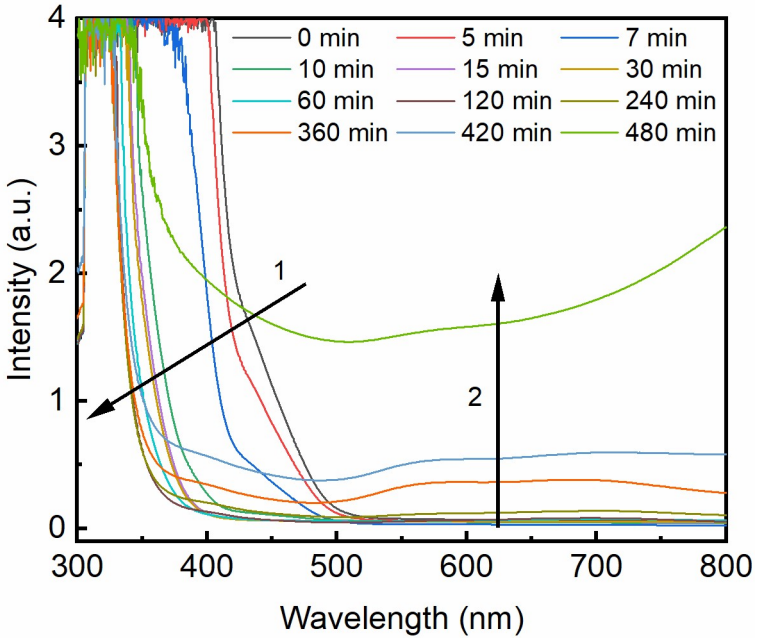

Figure S2. UV-vis absorption spectra changing of WCl_6 solution as alcoholysis reaction progresses.

The quickly decreased yellow absorption band within 10 min indicated the formation of $[W(OC_2H_5)_x]^{(6-x)+}$, and the gradually increased absorption in near infrared section implied the condensation reaction of these alcoholysis resultants.

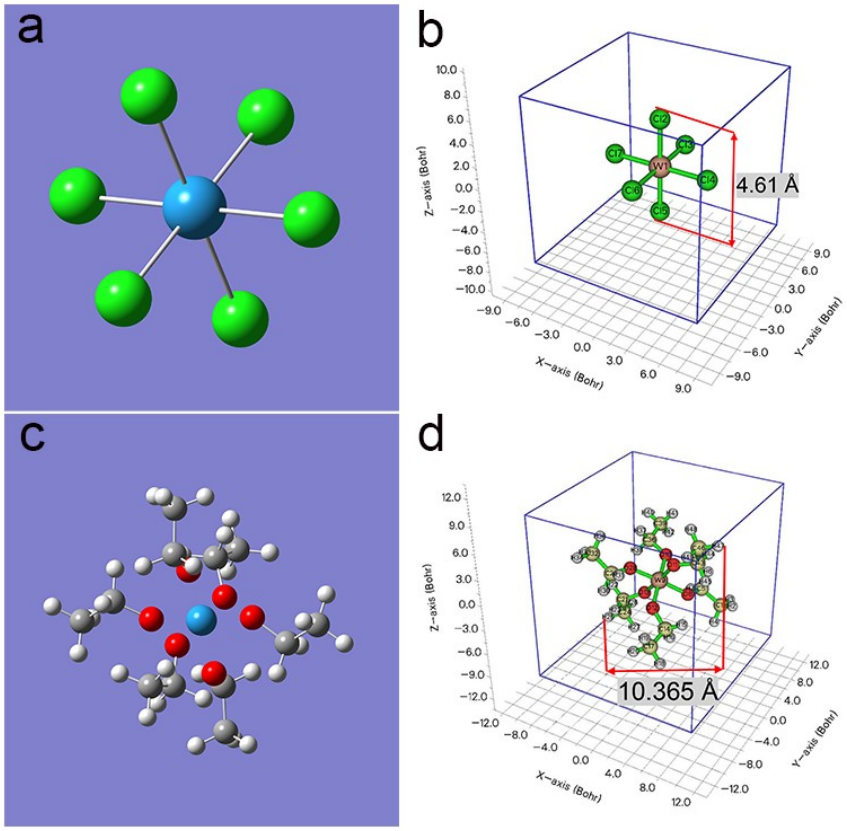

Figure S3. DFT calculated sizes of the tungsten precursors. (a) Model of the molecular structure of WCl_6 where blue sphere is W atom and the green spheres represent Cl atoms; (b) the calculated size of WCl_6 molecular; (c) model of the molecular structure of $W(OC_2H_5)_6$, the blue, red, grey and white spheres indicate W, O, C and H atoms, respectively; (d) the calculated size of $W(OC_2H_5)_6$ molecular. According to (b) and (d), the size of $W(OC_2H_5)_6$ molecular is obviously larger than that of WCl_6 molecular.

a. WCl_6 in pure EtOH:

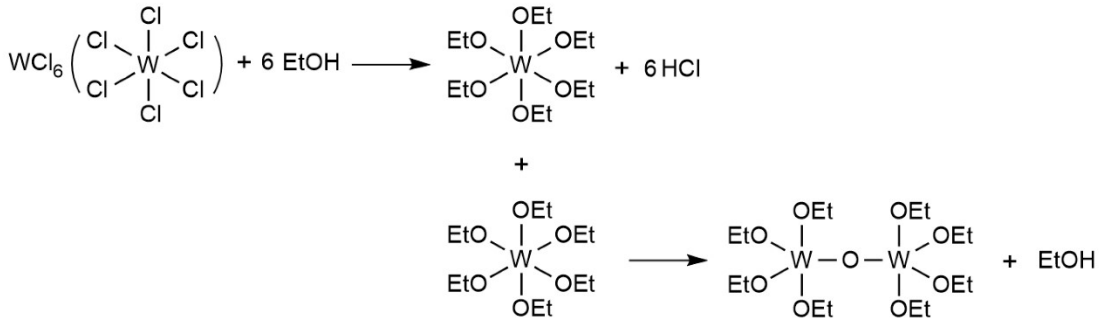

b. WCl_6 in pure acetone:

Figure S4. Reactions of WCl_6 with pure (a) EtOH and (b) acetone.

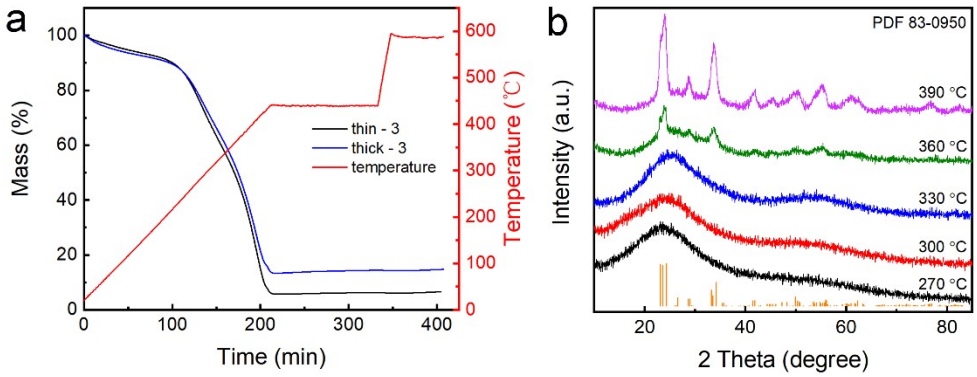

Figure S5. (a) Thermogravimetric (TG) curves of CMSs after absorption process. (b) XRD of CMSs after absorption calcinated at various temperatures.

The results in **Figure S2a** revealed that the amounts of metal ions adsorbed in the CMSs for thick-3 WO_3 HoMSs were larger than that in the CMSs for thin-3 WO_3 HoMSs. Experiments in **Figure S2b** were conducted under air atmosphere to mimic standard synthetic condition. The results indicated that the metal oxide was substantially formed at 270 °C.

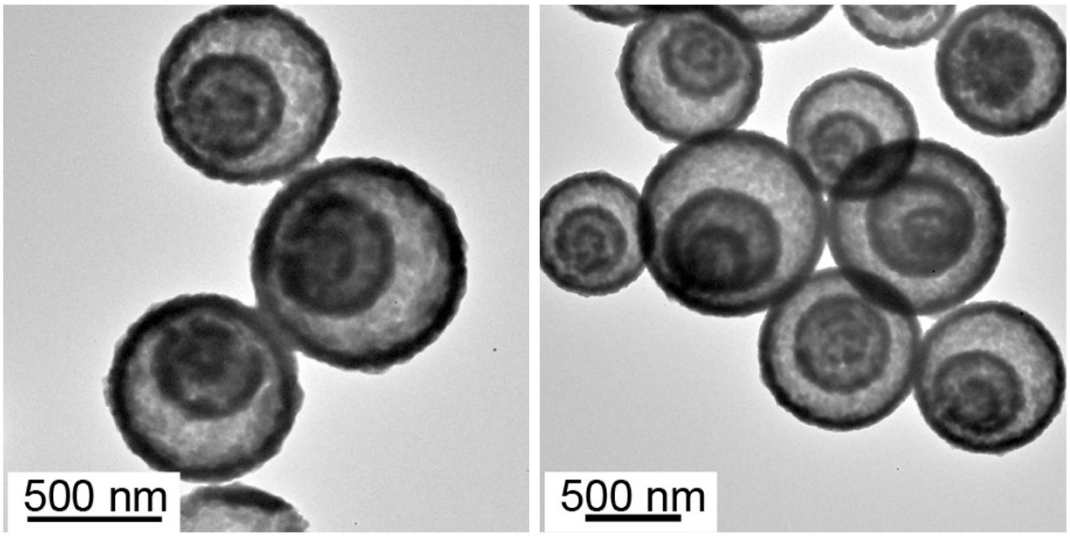

Figure S6. TEM images of triple shelled WO_3 HoMSs prepared by DMF and EtOH as solvent. Experimental details are showing in Table S2.

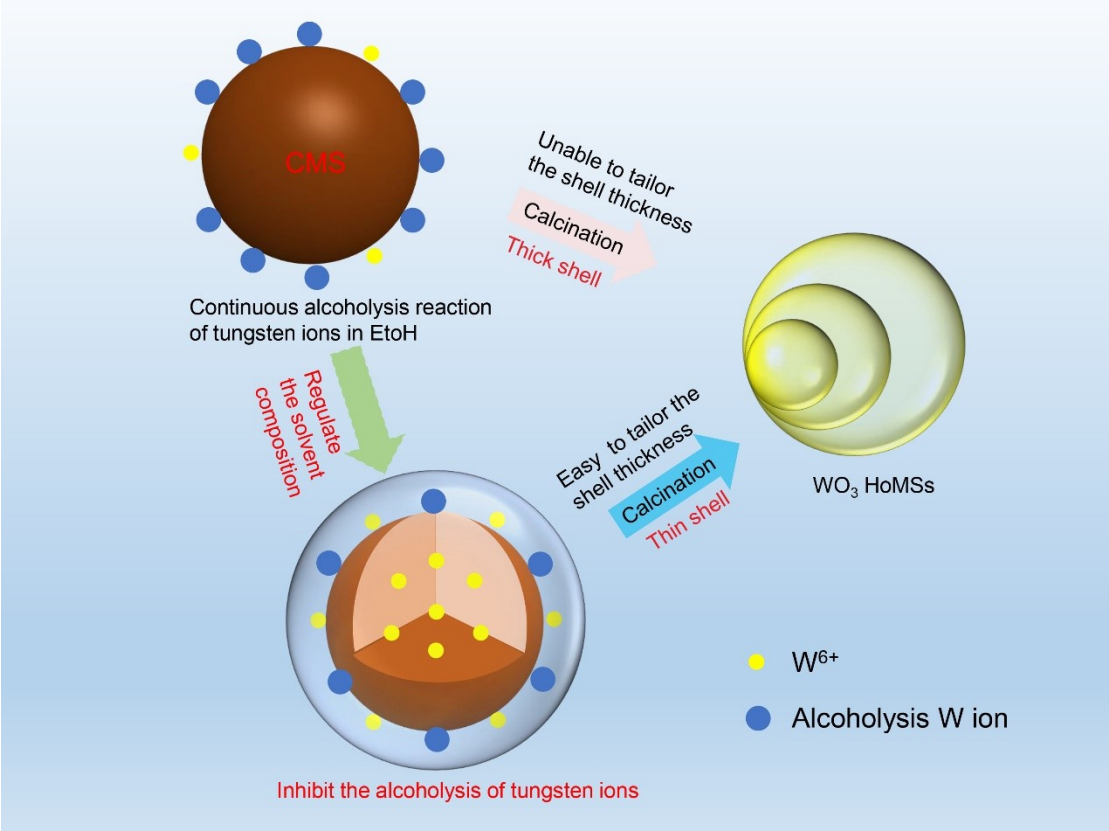

Figure S7. Schematic illustration of the solvent dominated adsorption process of CMSs templates for metal ions.

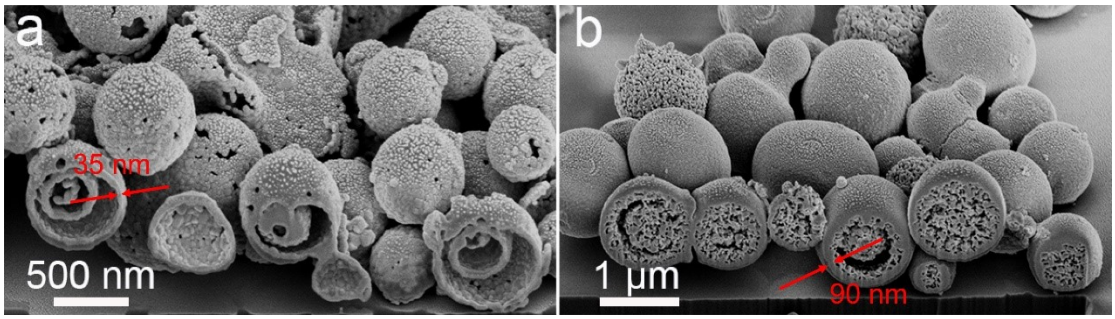

Figure S8. Large scale focused ion beam (FIB) - SEM images of the cross sections of (a) thin-3 and (b) thick-3 WO_3 HoMSs.

The adjacent shells in a WO_3 HoMS are contact, which is beneficial to promoting the transfer of photogenerated charge carriers.

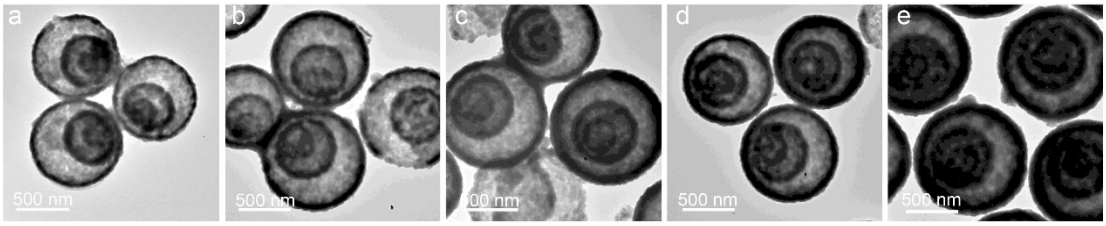

Figure S9. Regulation of the shell thickness by changing the solvent ratio and absorption duration. Average shell thicknesses of WO_3 HoMSs in (a-e) are 35. 45, 55, 65 and 80 nm, respectively.

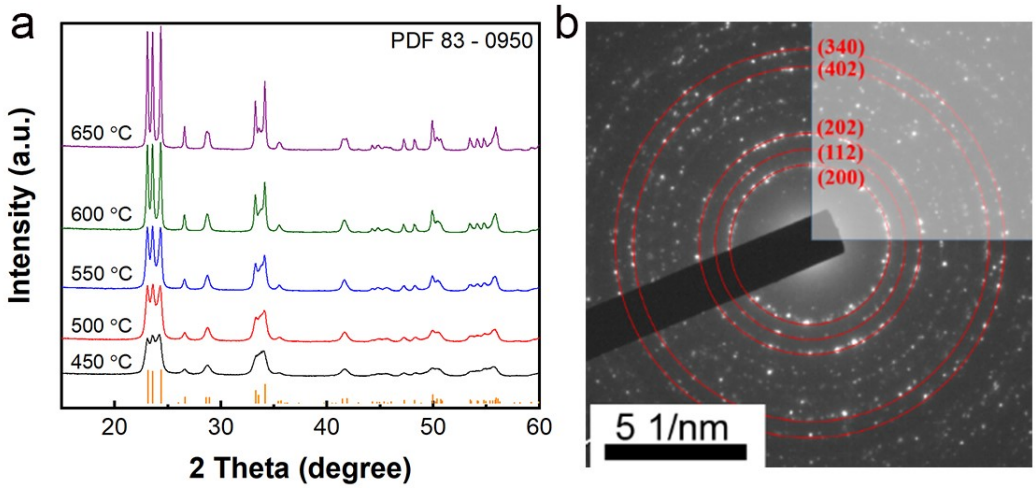

Figure S10. a) XRD patterns of WO_3 HoMSs calcinated under different temperatures. The crystallinity of WO_3 improved obviously as the calcination temperature increased. b) SAED image of thin triple-shelled WO_3 HoMSs prepared at 600 ºC.

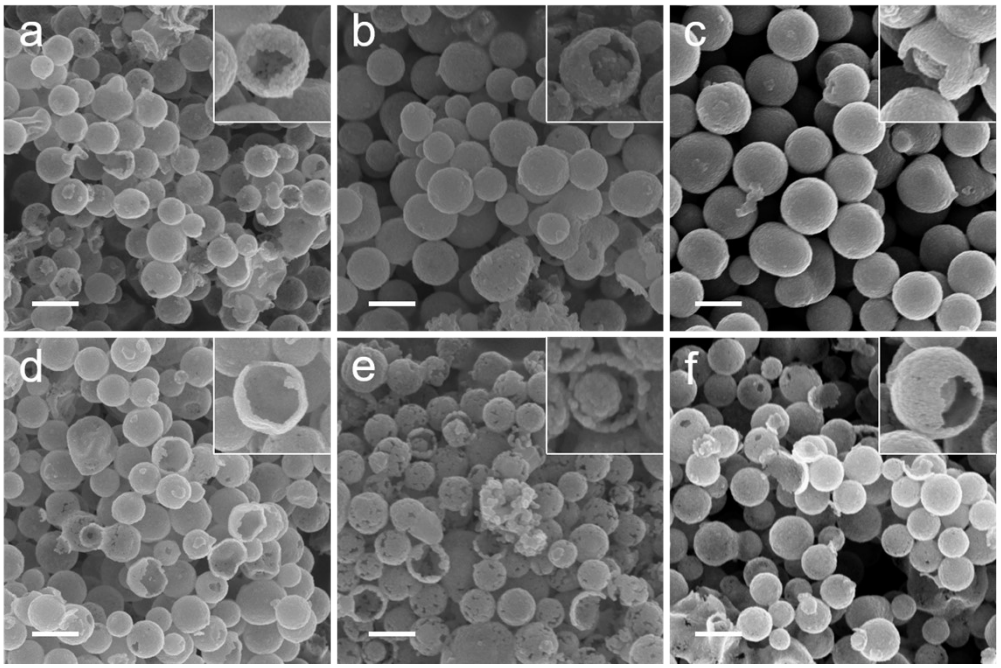

Figure S11. SEM images of as prepared samples. a) thick-1 WO_3 HoMSs, b) thick-2 WO_3 HoMSs, c) thick-3 WO_3 HoMSs, d) thin-1 WO_3 HoMSs, e) thin-2 WO_3 HoMSs, f) thin-3 WO_3 HoMSs, all insets show the high-magnification SEM images of typical microspheres. Scale bar, 1 μm.

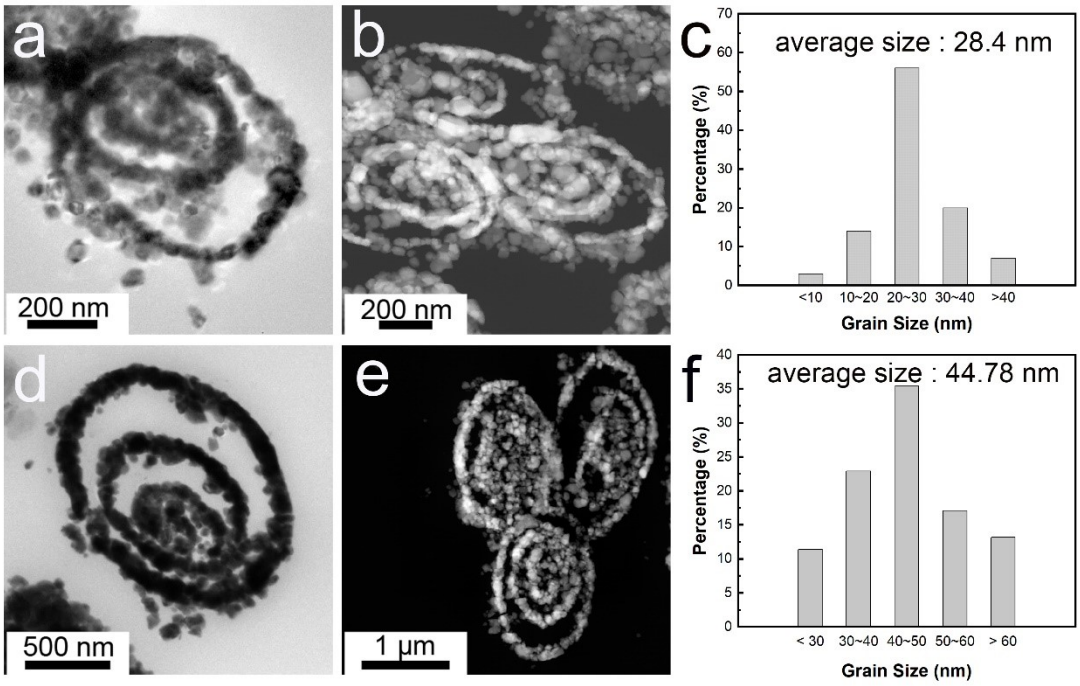

Figure S12. (a, b) TEM and STEM images of thin-3 WO_3 HoMSs slices, (c) is the size distribution of nanoparticles in thin-3 WO_3 HoMSs; (d, e) TEM and STEM images of thick-3 WO_3 HoMSs slices, (f) is the size distribution of nanoparticles in thick-3 WO_3 HoMSs.

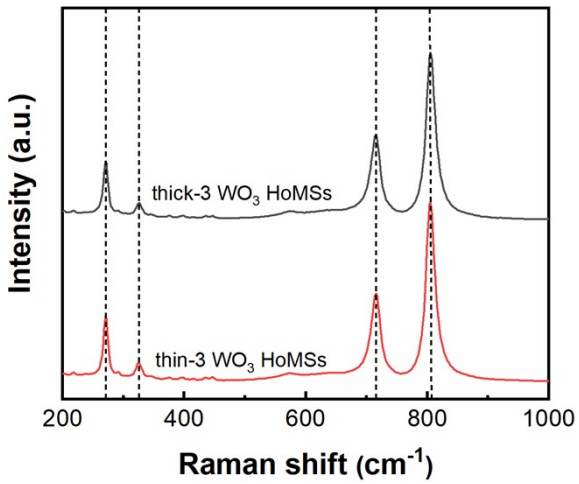

Figure S13. Raman spectra of thin-3 and thick-3 HoMSs.

The peaks at 270 cm^{-1}, 324 cm^{-1}, 715 cm^{-1} and 805 cm^{-1} are attributed to the bending and stretching mode of W-O-W of monoclinic structures. There is no apparent difference in the phase structure between different types of WO_3 hollow structures, which is consistent with XRD results.

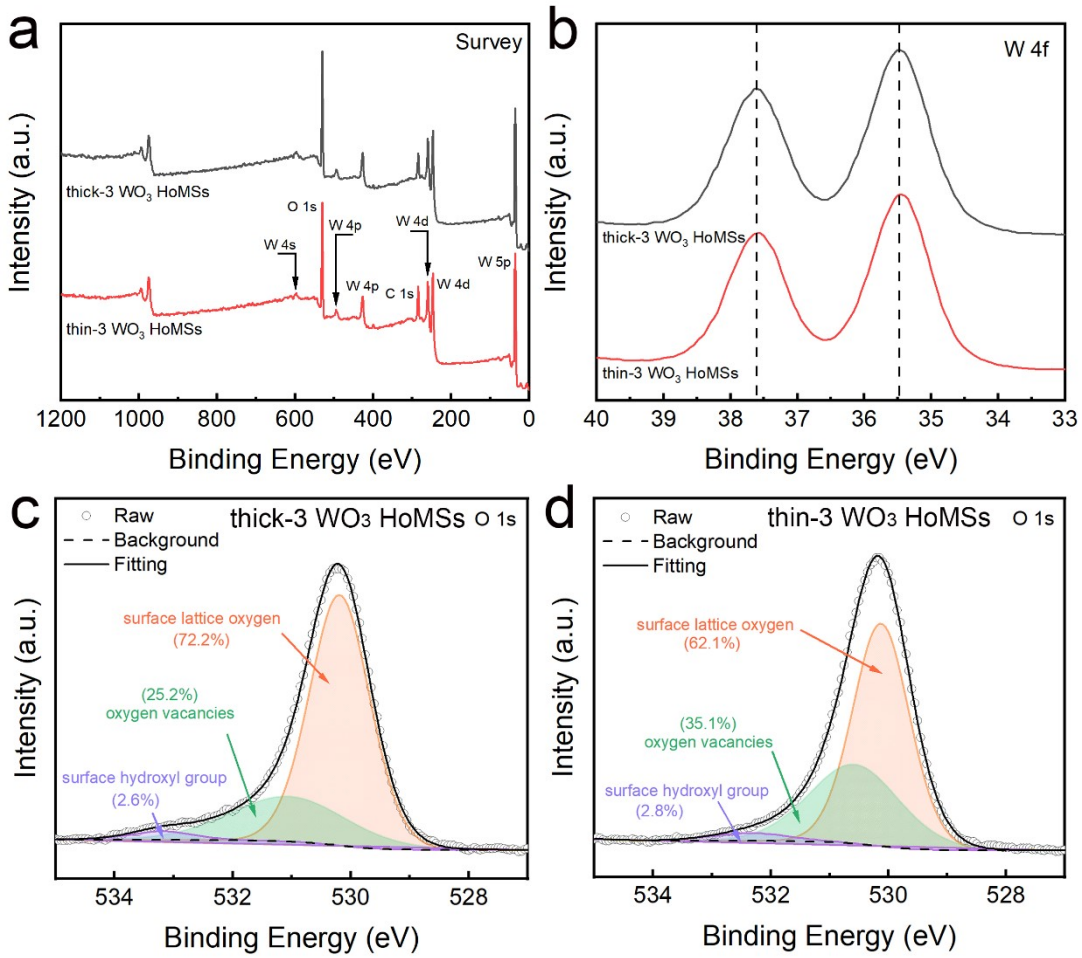

Figure S14. XPS spectra of thick- and thin-3 WO_3 HoMSs: (a) XPS survey spectra; (b) high-resolution XPS spectra of W 4f; (c) and (d) O1s orbitals of thick- and thin-3 WO_3 HoMSs.

These results suggest that the valence states and surface properties of thick- and thin-3 WO_3 HoMSs are similar. For O 1s XPS spectra of thick- and thin-3 WO_3 HoMSs, which can be deconvoluted into three peaks, including the peak of surface lattice oxygen species at 530.2 eV, the peak of oxygen vacancies at 531.06 eV and the peak of surface hydroxyl group at 533.2 eV. The ratio of oxygen vacancies in thin-3 WO_3 HoMSs (35.1%) is obvious larger than that in thick-3 WO_3 HoMSs (25.2%).

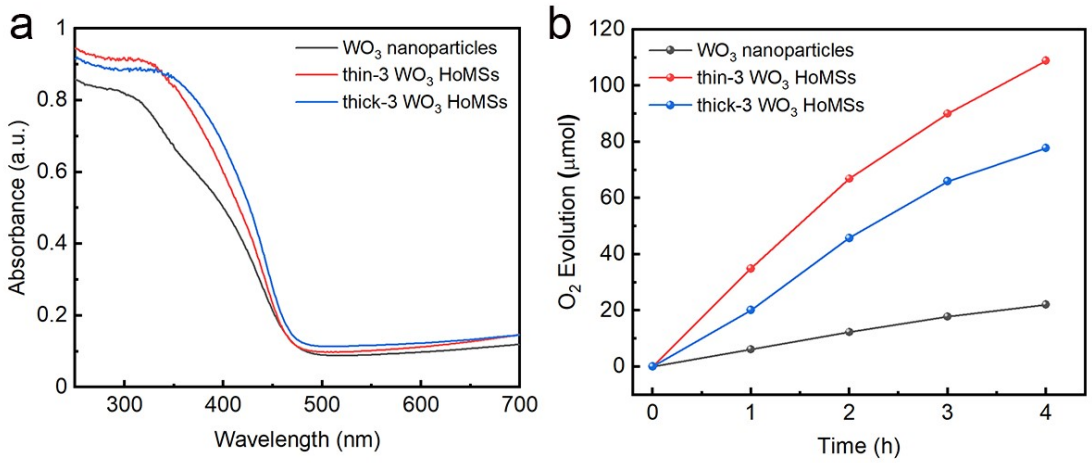

Figure S15. Comparison of (a) light-harvesting ability and (b) photocatalytic activities of WO_3 nanoparticles and WO_3 HoMSs.

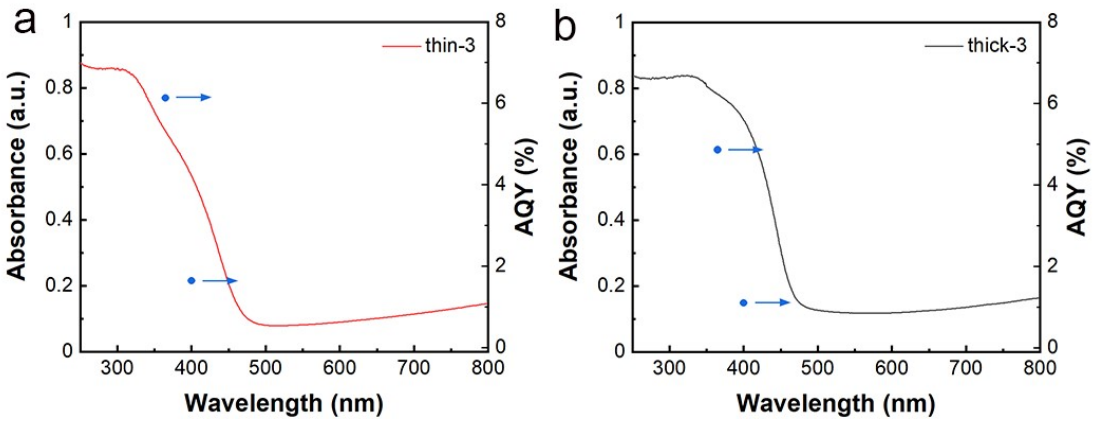

Figure S16. UV-vis absorption (left axis) spectrum and AQY plots (right axis) of (a) thin-3 and (b) thick-3 WO_3 HoMSs.

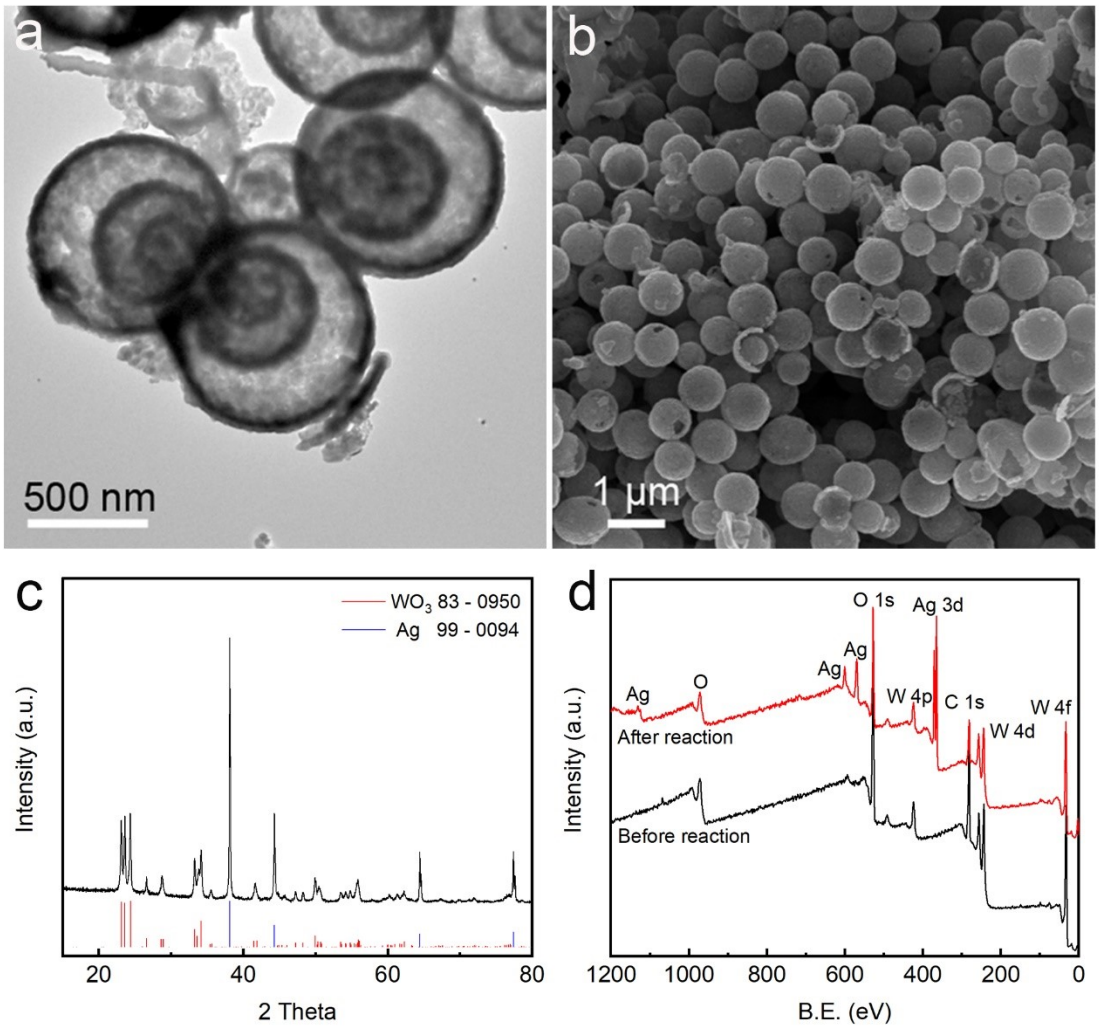

Figure S17. (a) TEM image, (b) SEM image, (c) XRD patterns and (d) XPS survey curves of thin-3 WO_3 HoMSs after photocatalytic test.

As shown in the picture above, the WO_3 HoMSs keep its initial structures without collapse after long-time reaction. Besides, crystal structure and chemical states of WO_3 HoMSs also remained stable.

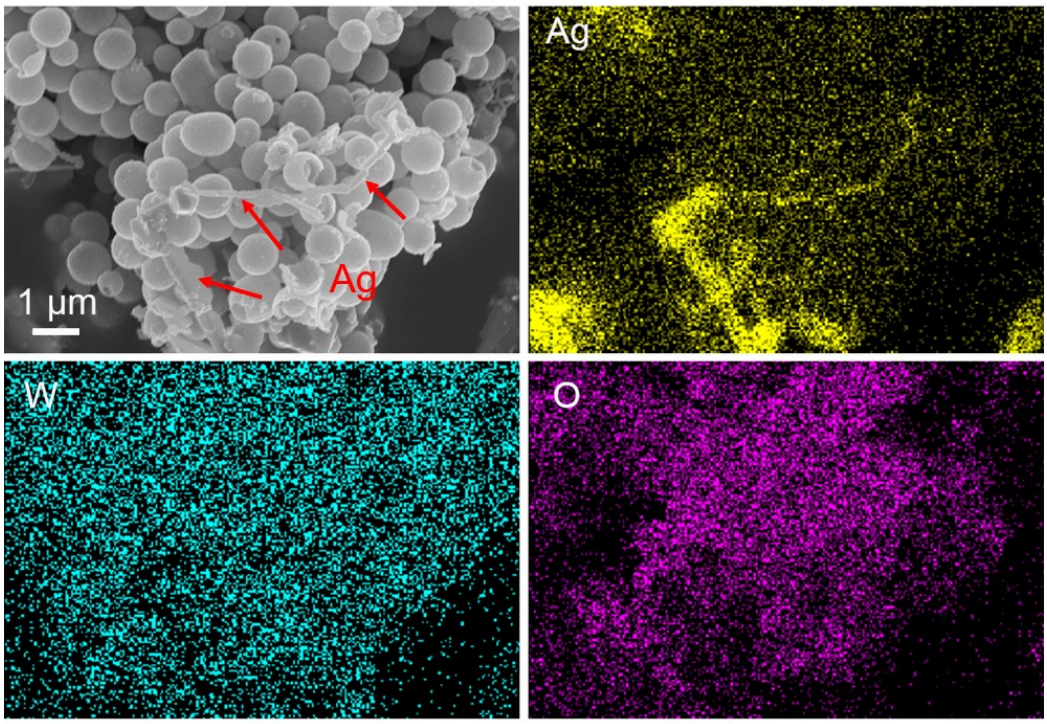

Figure S18. SEM images and elemental mapping of thin-3 WO_3 HoMSs after photocatalytic test.

The generated Ag is more inclined to self-assemble into nanowires or nanorods rather covering on the surface of WO_3 HoMSs.

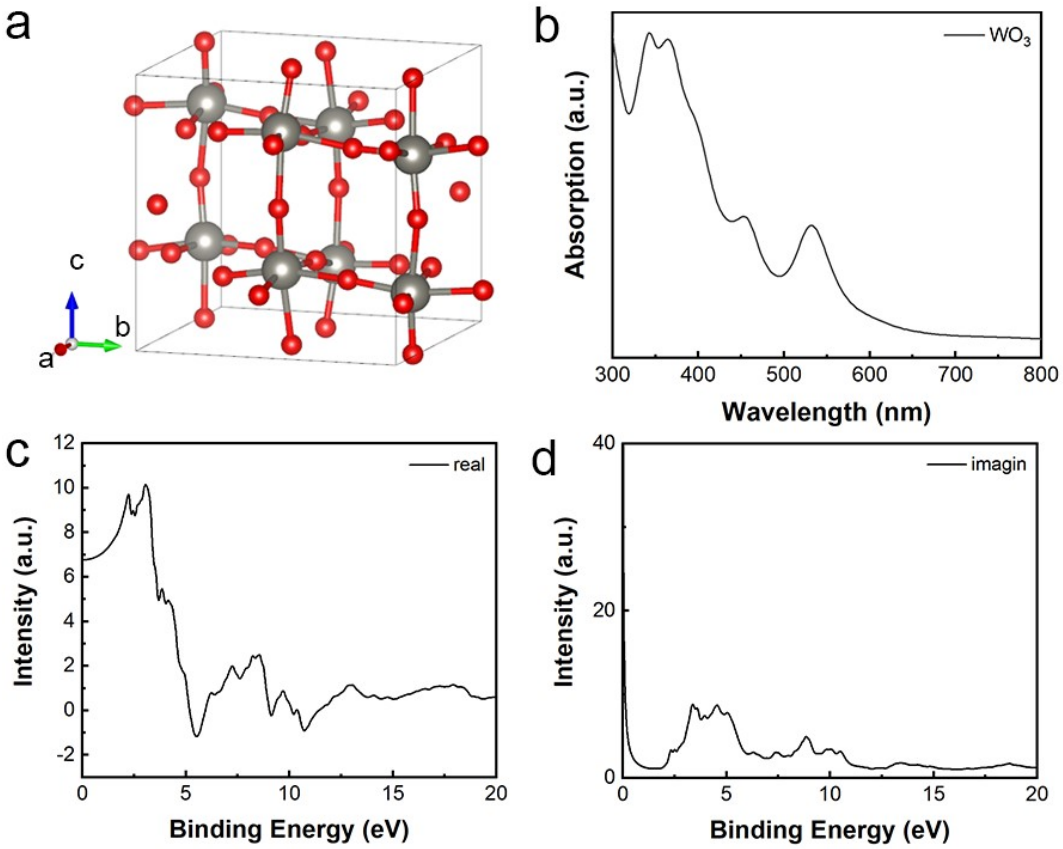

Figure S19. (a) Optimized crystal structure of WO_3 HoMSs. (b) Light absorption spectrum, (c) Real and (d) imaginary dielectric constant of WO_3 crystal obtained by first-principles calculations using the HSE06 functional.

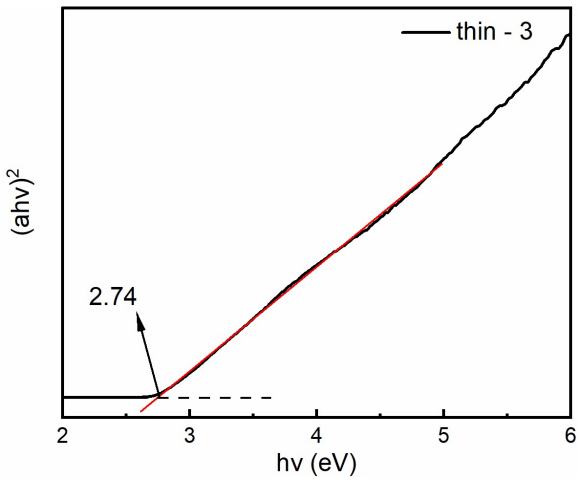

Figure S20. Tauc-plots of thin-3 WO_3 HoMSs.

The bandgap of thin-3 WO_3 HoMSs was calculated to be 2.74 eV, which is compliant with the value previous report.

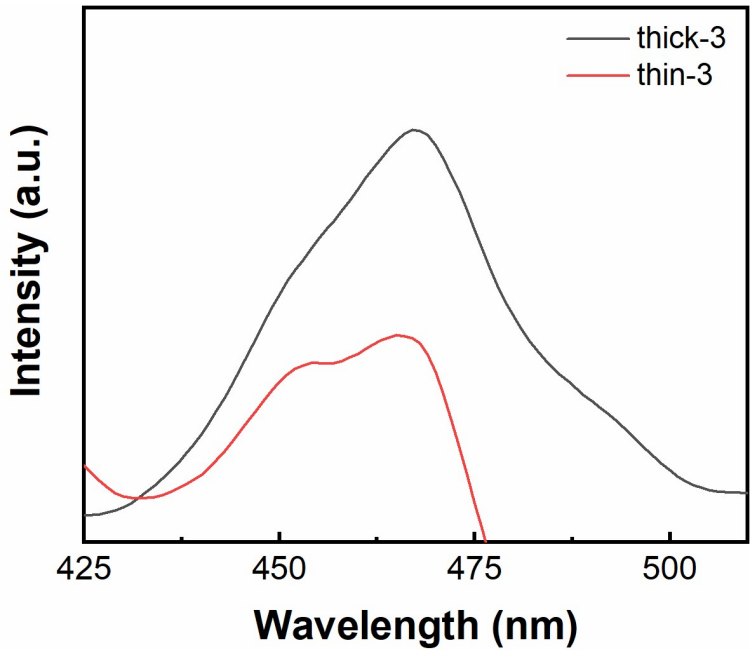

Figure S21. The steady-state PL emission spectra of thin-3 WO_3 HoMSs and thick-3 WO_3 HoMSs.

The photoluminescence (PL) spectra were recorded to investigate the separation efficiency of photogenerated carriers in triple-shelled WO_3 HoMSs with different shell thickness. The emission peak intensity of thick-3 WO_3 HoMSs is much stronger than that of thin-3 WO_3 HoMSs, which reveals the shell thickness has significant influence on the separation of photogenerated electron-hole pairs. The weak emission peak intensity of thin-3 WO_3 HoMSs indicates their lower charge-carrier recombination.

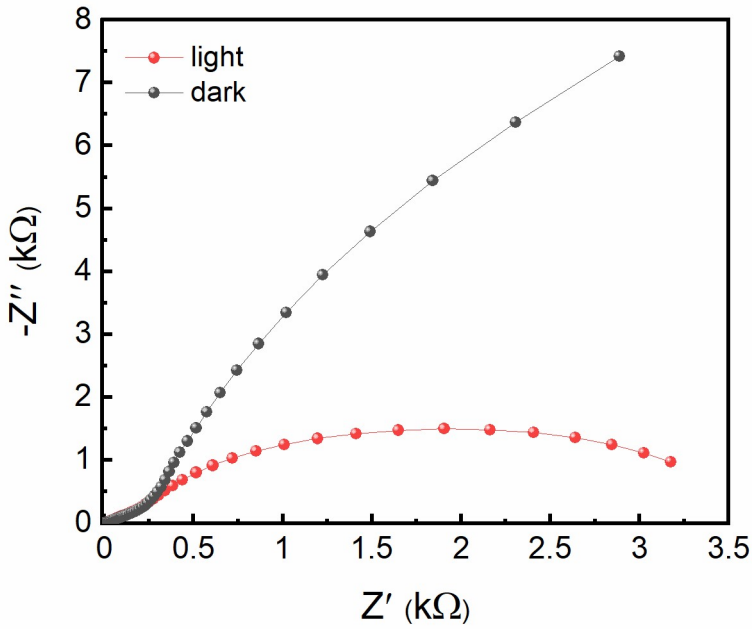

Figure S22. EIS Nyquist plots of thin-3 electrode measured in dark and visible-light irradiation in 0.5 M potassium phosphate buffer (pH = 7) solution.

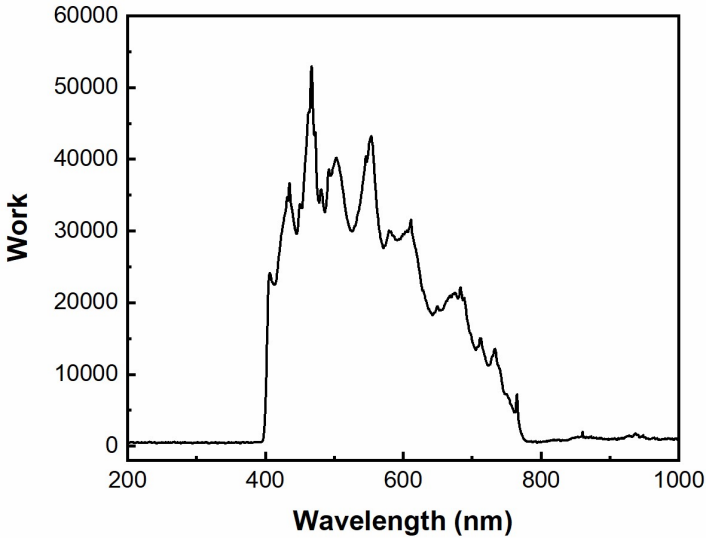

Figure S23. The power spectra of the 300 W Xe lamp equipped with a filter of visible light ($\lambda > 400$ nm).

Table S1. Summary of synthesis conditions for the WO_3 HoMSs

Structure types	thin-1	thin-2	thin-3	thick-1	thick-2	thick-3
Average shell thickness (nm)	20	20	35	50	60	90
Concentration of WCl_6 (M)	0.02	0.02	0.02	0.05	0.05	0.05
Solvent ratio (acetone/EtOH)	1:2	2:1	1:1	0:1	0:1	0:1
Adsorption temperature (°C)	25	25	25	25	40	50
Adsorption duration (h)	0.5	1	3	6	12	12
Calcination temperature (°C)	600	600	600	600	600	600

Table S2. Synthesis condition of WO_3 HoMSs when DMF was introduced.

Structure types	Concentration of WCl_6 (M)	Solvent	Adsorption temperature (ºC)	Adsorption duration	Calcination temperature (ºC)
WO_3 HoMSs	0.02	20 ml EtOH, 10 ml DMF	30	50 min	600

Table S3. Comparison of the shell thicknesses of thick-3 and thin-3 WO_3 HoMSs (Shell-1 indicates the outmost shell and shell-3 indicates the innermost shell).

Thickness (nm)	Shell-1	Shell-2	Shell-3
thick-3	90	55	45
thin-3	35	35	40

Table S4. N_2 sorption analysis results of thick-3 and thin-3 WO_3 HoMSs.

Sample	Specific surface area ($m^2\ g^{-1}$)	Average pore diameter (nm)	Total pore volume ($cc\ g^{-1}$)
Thick-3	40.957	9.819	0.153
Thin-3	62.438	13.292	0.136

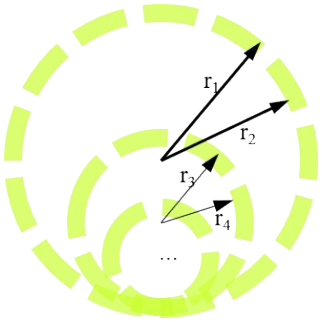

Scheme S1. A simple model of WO_3 HoMSs.

Table S5. Summary of structural parameters of thick-3 and thin-3 WO_3 HoMSs.

radius (nm)	r_1	r_2	r_3	r_4	r_5	r_6
thick-3	600	510	350	295	190	145
thin-3	385	350	215	180	100	60

$V_1 = \frac{4}{3}\pi (r_1^3 - r_2^3)$; $V_2 = \frac{4}{3}\pi (r_3^3 - r_4^3)$; $V_3 = \frac{4}{3}\pi (r_5^3 - r_6^3)$;

$V = V_1 + V_2 + V_3$

For thick-3 WO_3 HoMSs,

$V_{thick\text{-}3}\ \rho\ N_1 = m$,

where ρ is the density of WO_3, N_1 is the number of thick-3 WO_3 HoMSs, m is the weight of thick-3 WO_3 HoMSs.

For thin-3 WO_3 HoMSs,

$V_{thin\text{-}3}\ \rho\ N_2 = m$,

where ρ is the density of WO_3, N_2 is the number of thin-3 WO_3 HoMSs, m is the weight of thin-3 WO_3 HoMSs.

For the same weight of WO_3 HoMSs,

$V_{thick\text{-}3}\ \rho\ N_1 = V_{thin\text{-}3}\ \rho\ N_2$, therefore, $\frac{N2}{N1} = \frac{Vthick\text{-}3}{Vthin\text{-}3} = 5.47$

Namely, for the same weight of WO_3 HoMSs, the number of thin-3 WO_3 HoMSs is 5.47 times as high as that of thick-3 WO_3 HoMSs.

Table S6. Comparison of photocatalytic O_2 evolution performance of tungsten oxide-based photocatalysts in other works.

Catalyst	Sacrificial agent	Light source	Maximum OER rate ($\mu molg^{-1}h^{-1}$)	AQY	Ref
Thin-3 WO_3 HoMSs	$AgNO_3$ (0.01 M)	300 W Xe lamp ($\lambda > 400$ nm)	907	6.13% (365 nm)	This work
Thick-3 WO_3 HoMSs	$AgNO_3$ (0.01 M)	300 W Xe lamp ($\lambda > 400$ nm)	648.1	4.86% (365 nm)	This work
$WO_3/B_2O_{3-x}N_x$ nanoclusters	$AgNO_3$ (0.0185 M)	300 W Xe lamp ($\lambda > 400$ nm)	745	N/A	1
WO_3/RGO@Pt	KIO_3 (0.005 M)	150 W Xe lamp ($\lambda > 420$ nm)	87.46	3.4% (420 nm)	2
WO_3/H_xWO_3	$AgNO_3$ (0.01 M)	300 W Xe lamp ($\lambda > 420$ nm)	376.5	N/A	3
WO_3/Oxygen vacancy	$NaIO_3$ (0.01 M)	Xe lamp (AM 1.5)	1594	14.8% (350 nm)	4
Ru-WO_3	$NaIO_3$ (0.005 M)	300 W Xe lamp ($\lambda > 300$ nm)	65 $\mu mol\ h^{-1}$	N/A	5
WO_3/Oxygen vacancy	$AgNO_3$ (0.0118 M)	300 W Xe lamp ($\lambda > 420$ nm)	278.6	N/A	6
Pt@Cu_2O/ WO_3	$AgNO_3$ (0.01 M)	300 W Xe lamp	1238.6	1.2% (420 nm)	7
WO_3/Oxygen vacancy	$AgNO_3$ (0.029 M)	300 W Xe lamp ($\lambda > 400$ nm)	501.25	N/A	8
WO_3/Oxygen vacancy	$AgNO_3$ (0.01 M)	500 W Xe lamp (AM 1.5)	320	0.14% (420 nm)	9
WO_3/rGO	$AgNO_3$ (0.03 M)	300 W Xe lamp	580	N/A	10

WO_3/TiO_2	-	300 W Xe lamp ($\lambda > 420$ nm)	178	1.8% (420 nm)	11
Cs-WO_3	FeCl3 (0.004 M)	100 W LED lamp	51.3	3.7% (420 nm)	12
Pt/WO_3/Oxygen vacancy	$Na_2S_2O_8$ (0.1 M)	300 W Xe lamp	1037	N/A	13

References

1. Y. P. Xie, G. Liu, G. Q. Lu and H. M. Cheng, Boron oxynitride nanoclusters on tungsten trioxide as a metal-free cocatalyst for photocatalytic oxygen evolution from water splitting, *Nanoscale*, 2012, **4**, 1267-1270.
2. H. Huang, Z. Yue, G. Li, X. Wang, J. Huang, Y. Du and P. Yang, Ultraviolet-assisted preparation of mesoporous WO_3/reduced graphene oxide composites: superior interfacial contacts and enhanced photocatalysis, *J. Mater. Chem. A*, 2013, **1**.
3. G. Liu, J. Han, X. Zhou, L. Huang, F. Zhang, X. Wang, C. Ding, X. Zheng, H. Han and C. Li, Enhancement of visible-light-driven O_2 evolution from water oxidation on WO_3 treated with hydrogen, *J. Catal.*, 2013, **307**, 148-152.
4. J. Yan, T. Wang, G. Wu, W. Dai, N. Guan, L. Li and J. Gong, Tungsten oxide single crystal nanosheets for enhanced multichannel solar light harvesting, *Adv Mater*, 2015, **27**, 1580-1586.
5. H. Suzuki, S. Nitta, O. Tomita, M. Higashi and R. Abe, Highly Dispersed RuO_2 Hydrates Prepared via Simple Adsorption as Efficient Cocatalysts for Visible-Light-Driven Z-Scheme Water Splitting with an IO^{3-}/I^- Redox Mediator, *ACS Catal.*, 2017, 7, 4336-4343.
6 Q. Liu, F. Wang, H. Lin, Y. Xie, N. Tong, J. Lin, X. Zhang, Z. Zhang and X. Wang, Surface oxygen vacancy and defect engineering of WO_3 for improved visible light photocatalytic performance, *Catal. Sci. Technol.*, 2018, **8**, 4399-4406.
7. H. Gong, Y. Zhang, Y. Cao, M. Luo, Z. Feng, W. Yang, K. Liu, H. Cao and H.

Yan, Pt@Cu_2O/WO_3 composite photocatalyst for enhanced photocatalytic water oxidation performance, *Appl. Catal. B: Environ.*, 2018, **237**, 309-317.

8. J. Meng, Q. Lin, T. Chen, X. Wei, J. Li and Z. Zhang, Oxygen vacancy regulation on tungsten oxides with specific exposed facets for enhanced visible-light-driven photocatalytic oxidation, *Nanoscale*, 2018, **10**, 2908-2915.
9. Y. H. Chew, J. Y. Tang, L. J. Tan, B. W. J. Choi, L. L. Tan and S. P. Chai, Engineering surface oxygen defects on tungsten oxide to boost photocatalytic oxygen evolution from water splitting, *Chem. Commun.*, 2019, **55**, 6265-6268.
10. J. Ke, H. Zhou, J. Liu, Z. Zhang, X. Duan and S. Wang, Enhanced light-driven water splitting by fast electron transfer in 2D/2D reduced graphene oxide/tungsten trioxide heterojunction with preferential facets, *J Colloid Interface Sci*, 2019, **555**, 413-422.
11. X. An, Z. Shang, Y. Bai, H. Liu and J. Qu, Synergetic Photocatalytic Pure Water Splitting and Self-Supplied Oxygen Activation by 2D WO_3/TiO_2 Heterostructures, *ACS Sustainable Chem. Eng.*, 2019, **7**, 19902-19909.
12. D. Li, R. Chen, S. Wang, X. Zhang, Y. Zhang, J. Liu, H. Yin, F. Fan, J. Shi and C. Li, Unraveling the Kinetics of Photocatalytic Water Oxidation on WO_3, *J. Phys. Chem. Lett.*, 2020, **11**, 412-418.
13. Z. Wei, W. Wang, W. Li, X. Bai, J. Zhao, E. C. M. Tse, D. L. Phillips and Y. Zhu, Steering Electron–Hole Migration Pathways Using Oxygen Vacancies in Tungsten Oxides to Enhance Their Photocatalytic Oxygen Evolution Performance, *Angew. Chem. Int. Ed.*, 2021, **60**, 8236-8242.